Convective Storm Life Cycle and Environments near the Sierras de Córdoba, Argentina

JAKE P. MULHOLLAND, STEPHEN W. NESBITT, AND ROBERT J. TRAPP

Department of Atmospheric Sciences, University of Illinois at Urbana–Champaign, Urbana, Illinois

KRISTEN L. RASMUSSEN

Department of Atmospheric Sciences, Colorado State University, Fort Collins, Colorado

PAOLA V. SALIO

Department of Atmospheric and Oceanic Sciences, University of Buenos Aires, Buenos Aires, Argentina

(Manuscript received 8 March 2018, in final form 22 May 2018)

ABSTRACT

Satellite observations have revealed that some of the world's most intense deep convective storms occur near the Sierras de Córdoba, Argentina, South America. A C-band, dual-polarization Doppler weather radar recently installed in the city of Córdoba in 2015 is now providing a high-resolution radar perspective of this intense convection. Radar data from two austral spring and summer seasons (2015–17) are used to document the convective life cycle, while reanalysis data are utilized to construct storm environments across this region. Most of the storms in the region are multicellular and initiate most frequently during the early afternoon and late evening hours near and just east of the Sierras de Córdoba. Annually, the peak occurrence of these storms is during the austral summer months of December, January, and February. These Córdoba radar-based statistics are shown to be comparable to statistics derived from Tropical Rainfall Measuring Mission Precipitation Radar data. While generally similar to storm environments in the United States, storm environments in central Argentina tend to be characterized by larger CAPE and weaker low-level vertical wind shear. One of the more intriguing results is the relatively fast transition from first storms to larger mesoscale convective systems, compared with locations in the central United States.

1. Introduction

Satellite observations have revealed that some of the world's most intense thunderstorms occur across subtropical South America and, more specifically, in northern and central Argentina (e.g., Zipser et al. 2006; Romatschke and Houze 2010; Cecil and Blankenship 2012; Houze et al. 2015). These thunderstorms typically develop near a secondary mountain range to the east of the Andes called the Sierras de Córdoba (SDC), and they have been associated with severe weather hazards in the form of damaging straight-line wind gusts, large hail, flash flooding, and tornadoes (derived from local media and newspaper reports; Rasmussen and Houze 2011; Rasmussen et al. 2014). The production of severe weather has been shown to be strongly dependent upon the mode of convection (discrete vs multicellular; e.g., Dial et al. 2010), which is largely a factor of the vertical wind shear profile (e.g., Trapp 2013). Previous studies in the United States, such as Smith et al. (2012), have revealed that most tornado and large hail reports originate from supercellular convection, whereas damaging straight-line wind gusts predominantly occur with larger mesoscale convective systems. Similar studies have been largely absent across Argentina, however, as high spatiotemporal radar, surface, and upper-air observations are sparse, and a standard severe weather reporting procedure has not yet been implemented operationally at the time of this publication. The aim of the current study is to utilize data from a recently installed ground-based radar to characterize common convective life cycles near the SDC and establish a baseline climatology of environments supportive of this robust deep moist convection.

From an ingredients-based approach developed over the central United States (e.g., Johns and Doswell 1992;

Corresponding author: Jake P. Mulholland, jmulhol2@illinois.edu

DOI: 10.1175/MWR-D-18-0081.1

Doswell et al. 1996; Johnson and Mapes 2001), studies have linked severe thunderstorms to abundant lower-tropospheric moisture, steep midtropospheric lapse rates, and strong tropospheric vertical wind shear. The specific presence of tornadoes is particularly related to strong vertical wind shear over the lowest 1 km of the atmosphere and to lifting condensation levels below 1 km above ground level (AGL; e.g., Markowski et al. 2002; Thompson et al. 2003; Smith et al. 2012; Markowski and Richardson 2014). In subtropical South America, Brooks et al. (2003) and Rasmussen and Houze (2016) have shown that these ingredients are commonly present owing to the influence of midlatitude weather systems crossing the Andes, steep lapse rate midlevel air [elevated mixed layers (EMLs); Ribeiro and Bosart 2018], and abundant low-level moisture streaming poleward from the Amazon rainforest region in the South American low-level jet (SALLJ; Vera et al. 2006). Convection initiation (CI) typically occurs over the SDC owing to enhanced low-level moisture convergence and anabatic upslope flows.

Previous studies of deep convective storms across South America have predominantly used satellite data to elucidate details regarding storm structure and evolution (e.g., Nesbitt et al. 2006; Zipser et al. 2006; Rasmussen and Houze 2011; among others). Owing to the limitations of satellite data, specifically related to characterizing certain convective modes (e.g., supercells), along with the temporal evolution of the convection, this and other studies have been unable to understand the full convective mode spectrum and life cycle evolution in areas such as Argentina. Many of these limitations are mitigated with the installation of C-band, dual-polarization Doppler weather radars across Argentina to document convective-storm frequency, structure, and evolution in this region over multiple seasons. Until the present study, there have not been any systematic studies to examine convective modes, their life cycle, and their relationship to the ambient storm environments in this region, which motivates the work herein. As in prior studies, we identify common convective modes using newly available radar data from the C-band Córdoba radar (RMA1) during the austral springs and summers of 2015–17. A subjective storm classification scheme is used to identify prominent convective modes, including storm upscale convective growth into larger mesoscale convective systems. To quantify differences between the radar and satellite perspectives provided by the aforementioned prior works, life cycle statistics are compared to longer-term storm life cycle analyses using Tropical Rainfall Measuring Mission (TRMM) Precipitation Radar (PR) data from September 1998 to February 2014 over a similar domain. Finally, ERA-Interim composites are constructed for the RMA1-identified convective modes to further understand environments supportive of the observed convection. Section 2 outlines the data and methods used during this research. Section 3 provides the results from the radar, satellite, and composite analyses, and summary and conclusions are found in section 4.

TABLE 1. Córdoba radar specifications.

Type	C-band radar system (λ = 5.4 cm)
Frequency	5.6 GHz
Peak transmitted power	350 kW
Pulse duration	2 μs
Pulse repetition time	2000 μs
Range spacing	0.48 km
Maximum range	480 km
Beamwidth	0.98°
Polarization mode	Simultaneous transmit and receive
Recorded variables	Z, Z_{DR}, ρ_{HV}, V_R, spectral width, total differential phase, time series

2. Data and methods

a. Description of the Córdoba C-band radar system

RMA1 is a C-band (5.4-cm wavelength), dual-polarization Doppler weather radar that was installed in 2015 and is part of a new operational C-band network in Argentina. This radar system was designed and manufactured by INVAP–South America and is operated by the National System of Meteorological Radars (SINARAME; in Spanish) for the Servico Meteorólogico Nacional of Argentina. RMA1 records data at a range spacing of 480 m, with a maximum range of 480 km and a beamwidth of 0.98° (Table 1). RMA1 is a simultaneous transmit and receive dual-polarization radar (Table 1); however, within this study, dual-polarization data were not used, except for quality control (copolar correlation coefficient). RMA1 underwent upgrades during the month of November 2016, and thus, many events were likely missed during this time period as the radar was not operating (see Table 2).

RMA1 occasionally suffers from radio interference owing to its location within the large city of Córdoba, resulting in erroneous radar echoes (i.e., radial "spikes"). A simple quality-control filter was used in this analysis to remove most nonmeteorological echoes. Radar reflectivity and Doppler radial velocity data were masked out for this analysis if the reflectivity factor was <10 dBZ or copolar correlation coefficient ρ_{HV} was <0.7. Additionally, C-band radars are known to be subject to attenuation, differential attenuation, non-Rayleigh scattering, and backscatter differential phase effects when scanning regions of heavy rain/hail (Fabry 2015; Rauber and Nesbitt 2018); however, for the purposes of this study, these data were not corrected for these effects, as noncorrected data

TABLE 2. RMA1 number of days and 0.5° scans by month.

Month	Year	No. of days	No. of 0.5° scans
May	2015	22	3456
Jun	2015	26	4437
Jul	2015	26	3801
Aug	2015	28	5100
Sep	2015	28	3954
Oct	2015	30	2939
Nov	2015	28	5477
Dec	2015	27	2886
Jan	2016	25	3793
Feb	2016	23	3811
Mar	2016	30	3885
Apr	2016	28	3497
May	2016	25	4603
Jun	2016	0	0
Jul	2016	0	0
Aug	2016	0	0
Sep	2016	0	0
Oct	2016	28	1738
Nov	2016	19	1509
Dec	2016	26	12 012
Jan	2017	28	10 446
Feb	2017	27	10 027
Mar	2017	30	7948
Apr	2017	29	8561
May	2017	30	8975

were deemed adequate for convective cell tracking and mode classification.

b. *Córdoba radar storm tracking and classification*

Numerous studies have documented convective modes based upon a unique set of criteria. Most studies have utilized ground-based radar reflectivity signatures as a means of defining convective mode (e.g., Bluestein and Jain 1985; Houze et al. 1990; Klimowski et al. 2004; Trapp et al. 2005; Gallus et al. 2008; Schumann and Roebber 2010; Smith et al. 2012), and thus, a similar procedure has been implemented here.

Convective mode was separated into four categories: 1) multicell unorganized (MUN), 2) multicell organized (MCS), 3) discrete nonsupercell (DNS), and 4) discrete supercell (DSC). These categories were subjectively determined over a radar tracking analysis domain that was centered near the RMA1 site (31.44°S, 64.19°W; Fig. 1) and spanned 30°–33°S and 62.5°–66°W (approximately 300 km × 350 km in size).

With 0.5° radar reflectivity factor and Doppler radial velocity fields generated using the Python ARM Radar Toolkit (Py-ART; Helmus and Collis 2016), the aforementioned convective mode categories were further restricted by the following criteria (see Figs. 2, 3):

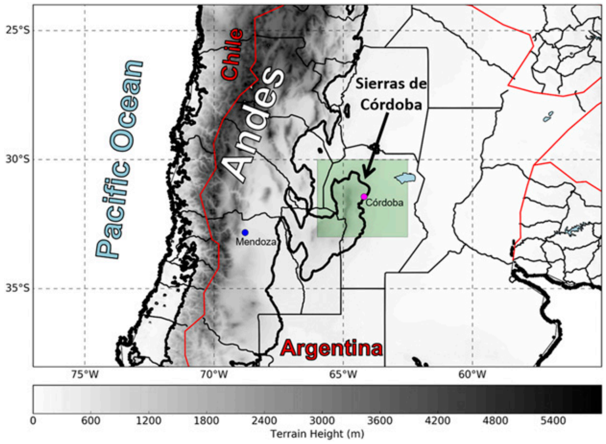

FIG. 1. Córdoba radar tracking domain (30°–33°S, 62.5°–66°W; green box), terrain height (shaded in gray; m), national borders (red line), and the 500-m elevation contour (thick black line).

1) The MUN events had to display cells that were ≤25 km from one another with reflectivity ≥30 dB*Z*.
2) The MCS events had to display a region of contiguous reflectivity ≥30 dB*Z* over a horizontal distance of ≥50 km and contain at least one ≥50 dB*Z* reflectivity core.
3) The DNS events had to display non- or weakly rotating cells that were >25 km apart from one another with reflectivity ≥30 dB*Z*.
4) The DSC events had to display clear rotation (assessed using 0.5° radial velocity data) for ≥15 min with reflectivity ≥30 dB*Z* and were typically associated with reflectivity hook echoes, especially closer to the radar (cf. Fig. 3a).

Each of these convective modes was based upon the dominant mode throughout the event [e.g., after Gallus et al. (2008)]. The dominant convective mode was defined as the mode that lasted the longest, or displayed the highest degree of organization (e.g., Schumann and Roebber 2010), throughout an event. Convective cells that were difficult to bin into one of the four above categories were grouped into either the MUN or DNS categories, depending on their presence as a time fraction of the overall convective mode of an event. An "event" was defined as the time interval from convection initiation to system demise, or the time interval over which convection (i.e., reflectivity ≥30 dB*Z*) entered and exited the domain; CI was defined as the first appearance of a ≥30-dB*Z* echo (at the 0.5° scan angle) over at least five radar gates. If two (or more) different instances of CI occurred on the same day, these were partitioned into two separate events. Events that featured storms that moved into the lateral boundaries of the tracking domain, or lacked radar data at the time of CI, were binned into a separate category.

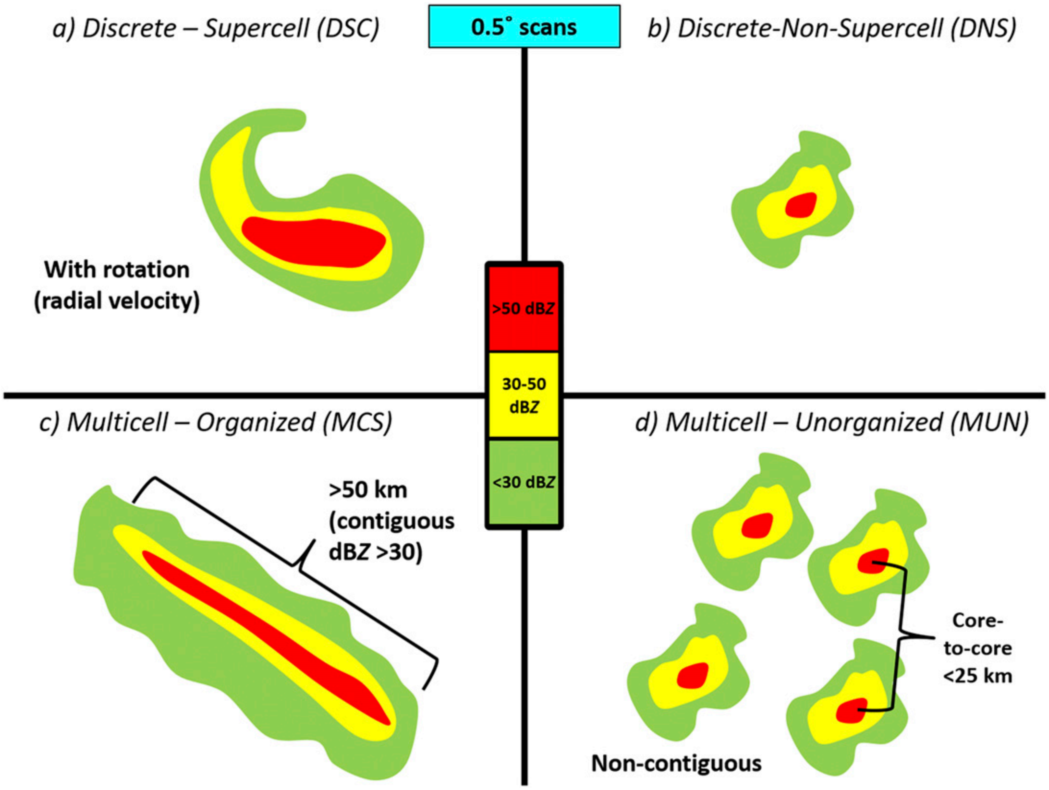

FIG. 2. Idealized schematic of the four convective modes that were defined for the Córdoba radar tracking: (a) DSC, (b) DNS, (c) MCS, and (d) MUN. The shading corresponds to base radar reflectivity (dBZ).

Additionally, any instances of upscale convective growth into an MCS (e.g., through a presumed amalgamation of cold pools) from MUN, DNS, or DSC convective modes were noted (independent of the dominant convective mode characterization). In the context of this study, upscale convective growth was defined as the instant when the length of the contiguous ≥30-dBZ radar echo spanned at least 50 km horizontally with ≥50-dBZ embedded cores.

c. *TRMM Precipitation Radar storm identification and classification*

TRMM PR satellite data version 7 (v7; TRMM data accessed from http://trmm.atmos.washington.edu/) were used in this study to compare with the RMA1 analyses, with the caveat being that the TRMM PR analyses are "snapshots" in time, while the ground-based radar provides a temporal characterization of the convection. TRMM PR data have coarse horizontal, but relatively fine vertical, resolution of 4–5 km and 250 m, respectively, with an average horizontal swath width of ~220 and 250 km before and after 7 August 2001, respectively (Kummerow et al. 1998). Events were identified between September 1998 and February 2014 over the same tracking domain as the RMA1-identified storms (green box in Fig. 1) and were binned into the months of September–November (SON; austral spring) or December–February (DJF; austral summer). These events were categorized by convective mode in a similar fashion as the RMA1 events; however, owing to the inability of the TRMM PR to deduce rotation within convection, DSC and DNS events (which were defined during the RMA1 tracking) were combined into a single category—"discrete" storms—for the subsequent set of TRMM PR analyses. Rasmussen and Houze (2011) demonstrate that the TRMM PR satellite can discern multicell systems quite well, and thus, the MCS and MUN categories remain partitioned for both the TRMM PR and RMA1 tracking. Furthermore, these satellite-identified events were separated into wide convective core (WCC; areal extent of 40-dBZ echo >1000 km^2) and deep convective core (DCC; height of 40-dBZ echo >10 km) categories based upon the classification scheme outlined by Houze et al. (2007). Example events, including vertical cross sections, of the three convective mode categories defined for the TRMM PR analyses are depicted in Fig. 4.

d. *ERA-Interim composites*

ERA-Interim data (Dee et al. 2011) were utilized to characterize the ambient, synoptic-scale environment

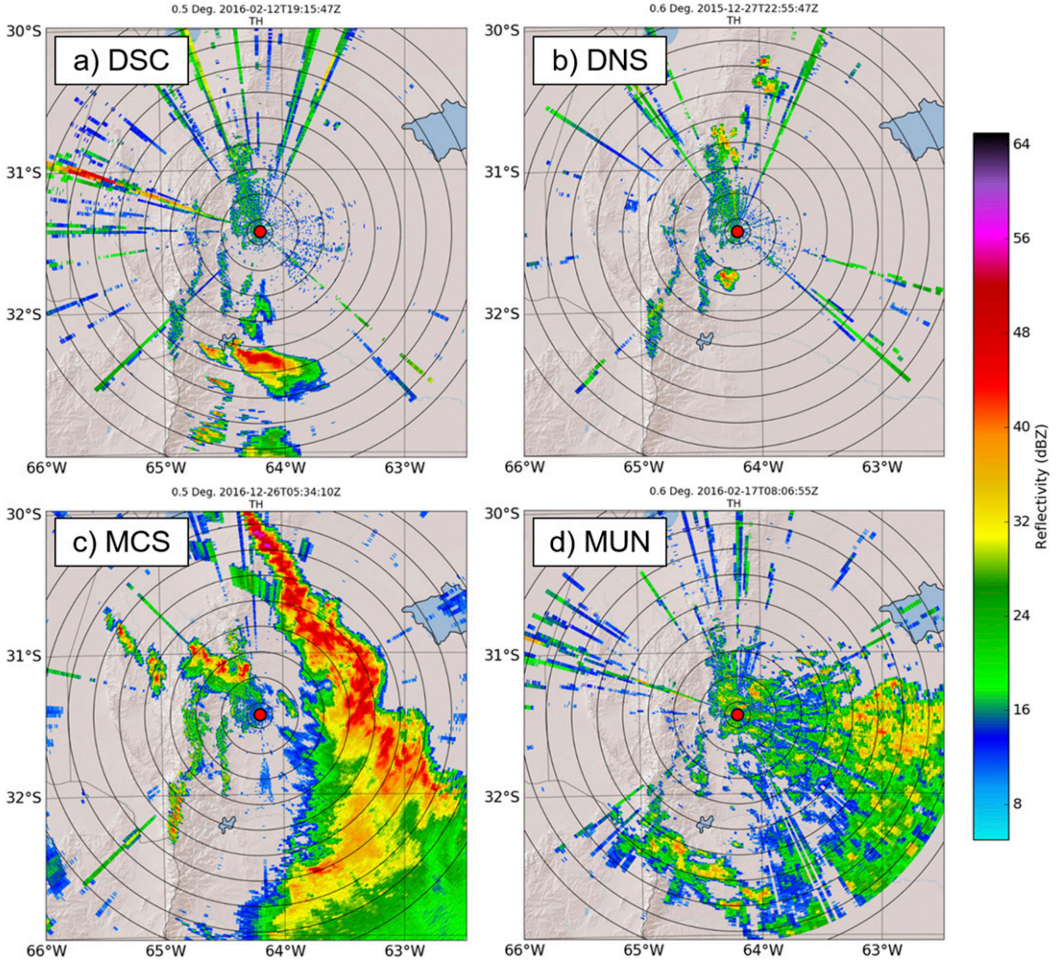

FIG. 3. Example events of the four convective modes that were defined for the Córdoba radar tracking: (a) DSC (1915 UTC 12 Feb 2016), (b) DNS (2255 UTC 27 Dec 2015), (c) MCS (0534 UTC 12 Dec 2016), and (d) MUN (0806 UTC 17 Feb 2016). The shading denotes 0.5° radar reflectivity (dB*Z*), the red dot denotes the location of the Córdoba radar, and the range rings are spaced every 20 km, with the first range ring from the radar at 10 km.

for convective modes identified from the RMA1 data. ERA-Interim is a global (atmospheric) reanalysis dataset produced by the European Centre for Medium-Range Weather Forecasts (ECMWF). ERA-Interim includes 3-h surface data and 6-h upper-air data and utilizes four-dimensional variational data assimilation techniques. The horizontal grid spacing is 0.7° (approximately 80 km) with 37 vertical model levels (P_{top} = 1 hPa); pressure-level interpolated data were used for this analysis.

Reanalysis data were used to construct composites of synoptic-scale fields, such as 250-hPa height/wind, 850-hPa moisture/wind, mixed-layer convective available potential energy (MLCAPE; averaged over the lowest 100 hPa), mixed-layer convective inhibition (MLCIN; averaged over the lowest 100 hPa), deep-layer and low-level vertical wind shear (calculated as a bulk wind difference between 0 and 6, 0 and 3, and 0 and 1 km AGL), storm-relative helicity (SRH; Davies-Jones 1984; 0–3 and 0–1 km AGL), and others, across the north-central Argentine region for the four dominant convective mode categories defined for the RMA1 tracking. Additionally, violin box plots were constructed from the ERA-Interim dataset for relevant severe weather indices averaged over the RMA1 tracking domain centered on the RMA1 site utilizing the Sounding and Hodograph Analysis Program in Python (SHARPpy; Blumberg et al. 2017). The reanalysis surface data (2-m air temperature, 10-m winds) were inserted using surface pressure in the pressure-level data before constructing model soundings at each grid point.

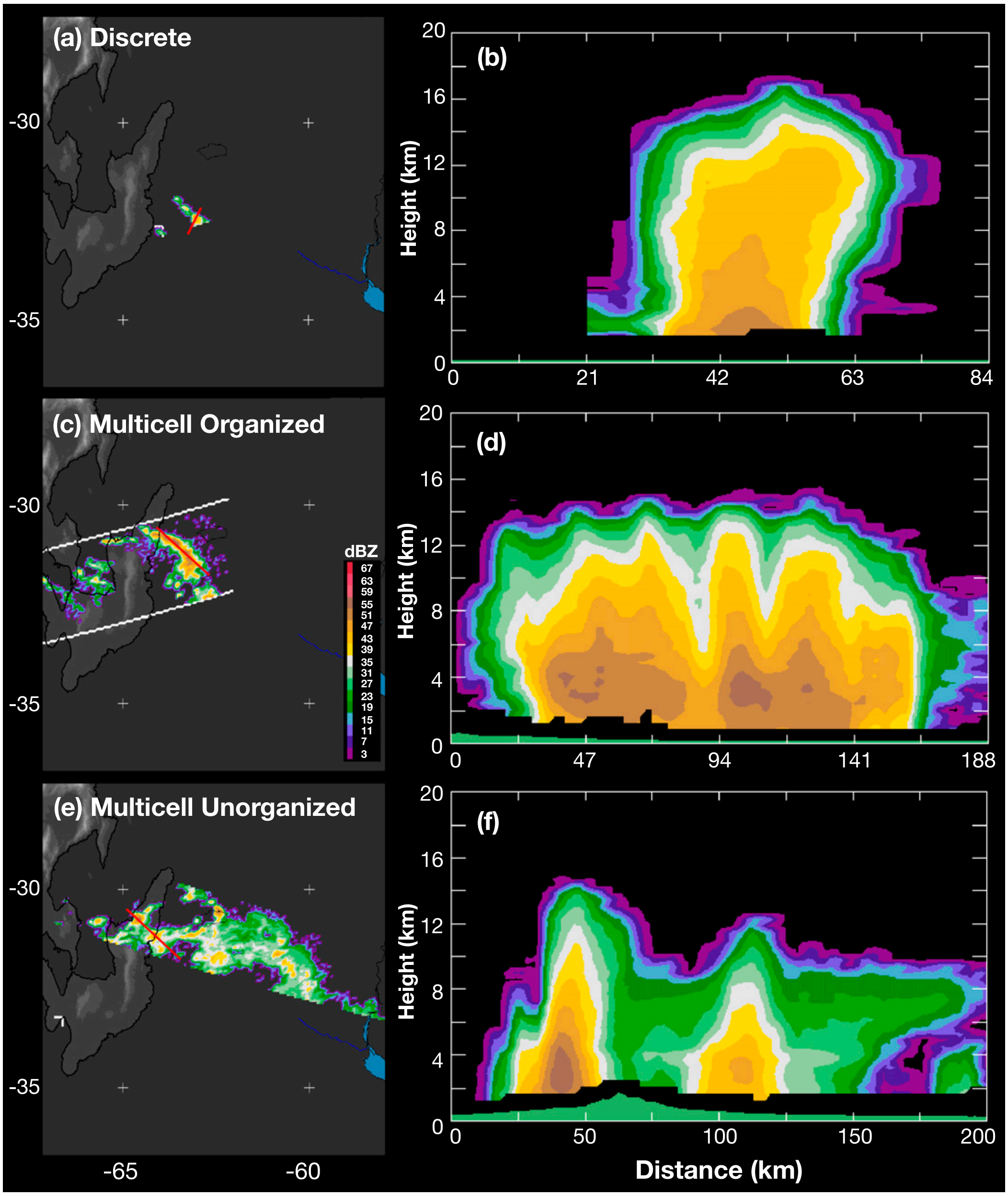

FIG. 4. Example events identified by the TRMM PR of the (a),(b) discrete (2026 UTC 22 Oct 1998); (c),(d) multicell-organized (0321 UTC 12 Dec 2001); and (e),(f) multicell-unorganized (0418 UTC 15 Nov 1998) convective modes. (b),(d),(f) Vertical cross sections taken along the red line in (a),(c),(e), respectively. The radar reflectivity (dBZ) values in all panels are the same.

3. Results

a. Córdoba radar storm tracking statistics

A total of 183 storm events were identified between May 2015 and May 2017, documenting different convective modes and subsequent upscale convective growth (if applicable). All 183 events were grouped by (any) convective mode present during the event, dominant convective mode throughout the event, CI location/time (within the domain), and time between CI and upscale convective growth (if any). In terms of dominant convective mode, 66 (36%) of the events were characterized as MUN, 57 (31%) as MCS, 41 (22%) as DNS, and 19 (11%) as DSC. This distribution in convective mode, with ~67% multicell events and ~33% discrete events, is similar to studies of convection across the central United States (e.g., Schumann and Roebber 2010).

Of the 183 events, 113 had radar data available at the time of CI and additionally had CI within the tracking

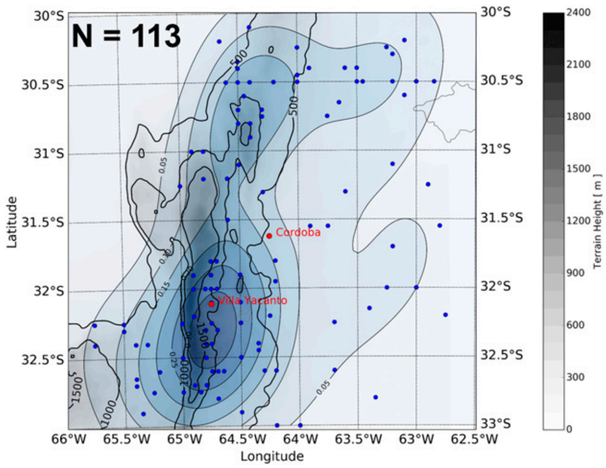

FIG. 5. Spatial distribution of all 113 CI locations (blue dots) and a kernel density estimation (KDE; using Scott's rule; Scott 1992) of these locations (blue shades). KDE contours are thin black lines every 0.05, starting at 0.05. The cities of Córdoba and Villa Yacanto are labeled in red. Terrain contours of 500, 1000, and 1500 m are outlined in thick black lines, and terrain height is shaded in gray (m).

domain. Most CI events tend to cluster over the steepest gradient in terrain of the SDC, near the city of Villa Yacanto (Fig. 5). There is also a secondary peak in CI to the north-northwest of Córdoba. CI additionally occurs over the lower elevations to the east of the SDC, but this is relatively less frequent, compared with the number of CI events over the SDC.

All of the CI events were partitioned by their dominant convective mode throughout the lifetime of the event and traced backward to CI location. MCS (Fig. 6a) and DSC (Fig. 6c) events tend to have CI locations that are near the city of Villa Yacanto, while DSC CI events are clustered over the higher terrain. The DNS events (Fig. 6d) almost exclusively initiate over the SDC, whereas the MUN events (Fig. 6b) display two main CI centroids, with one maximum near and southwest of Villa Yacanto and a secondary maximum along the northern tip of the SDC (near 30.75°S, 64.25°W). Additional MUN events have CI well to the east of Córdoba, across the lower elevations (Fig. 6b).

There is a distinct bimodal structure in the temporal distribution of CI, with the first peak in CI occurring between ~1400 and 1900 UTC (1100–1600 LST) and the second peak occurring between ~2300 and 0600 UTC (2000–0300 LST; Fig. 7). There is a minimum in CI that occurs during the early dawn (0700–1300 UTC; 0400–1000 LST) and the midafternoon hours (2000–2300 UTC; 1700–2000 LST). This bimodal structure in CI time in this region has been identified in previous studies of South American MCS events (e.g., Salio et al. 2007; their Fig. 3, bottom-left panel). The first peak in CI is likely a result of diurnal heating of the SDC and resultant anabatic upslope flows, which subsequently converge on the ridgeline. The secondary peak is more challenging to understand and has not received much study to date, but we hypothesize that a nocturnal acceleration of the SALLJ (e.g., Bonner 1968; Repinaldo et al. 2015) results in enhanced low-level moisture convergence near the unique terrain of the SDC, thus fostering CI there. Furthermore, nocturnal slope flows interacting with the SALLJ could be another potential catalyst for additional CI to occur.

The annual distribution of all 183 events for RMA1 and 372 events for the TRMM PR (also see section 3b) is depicted in Fig. 8, with the number of events from the RMA1 dataset normalized in the following way:

$$(\text{total number of days in month} - \text{days with available radar data}) \\ \times (\text{total number of storm counts in that particular month}).$$

This normalization method was used to account for periods when RMA1 was not operating (see Table 2). The austral winter months of May–September were characterized by the fewest number of events, with a large increase in events between October and February (austral spring into summer). The maximum number of RMA1-identified events (~36) occurred in February (some days have multiple events), whereas the maximum number of TRMM PR-identified events (~95) occurred in November. This RMA1 distribution matches well with the analyses of TRMM PR-identified storms from Rasmussen and Houze (2011; their Fig. 5a for the SDC region) and the TRMM PR storm counts for this study (section 3b). MCS events had two peaks, with one in November (nine events) and another in January (14 events; Fig. 9). DNS events had an increase in number between October (one event) and January/February (10 events; Fig. 9). The MUN events had a fairly uniform distribution, with a 3-month peak of 10 events between December and February (Fig. 9). Similar to the MCS events, DSC events had two main peaks. The first peak was in November (four events), whereas the second peak was in February (six events; Fig. 9). Overall, there was a tendency for more discrete convective modes earlier in the austral spring season (October–December) and more multicellular convective modes later in the austral

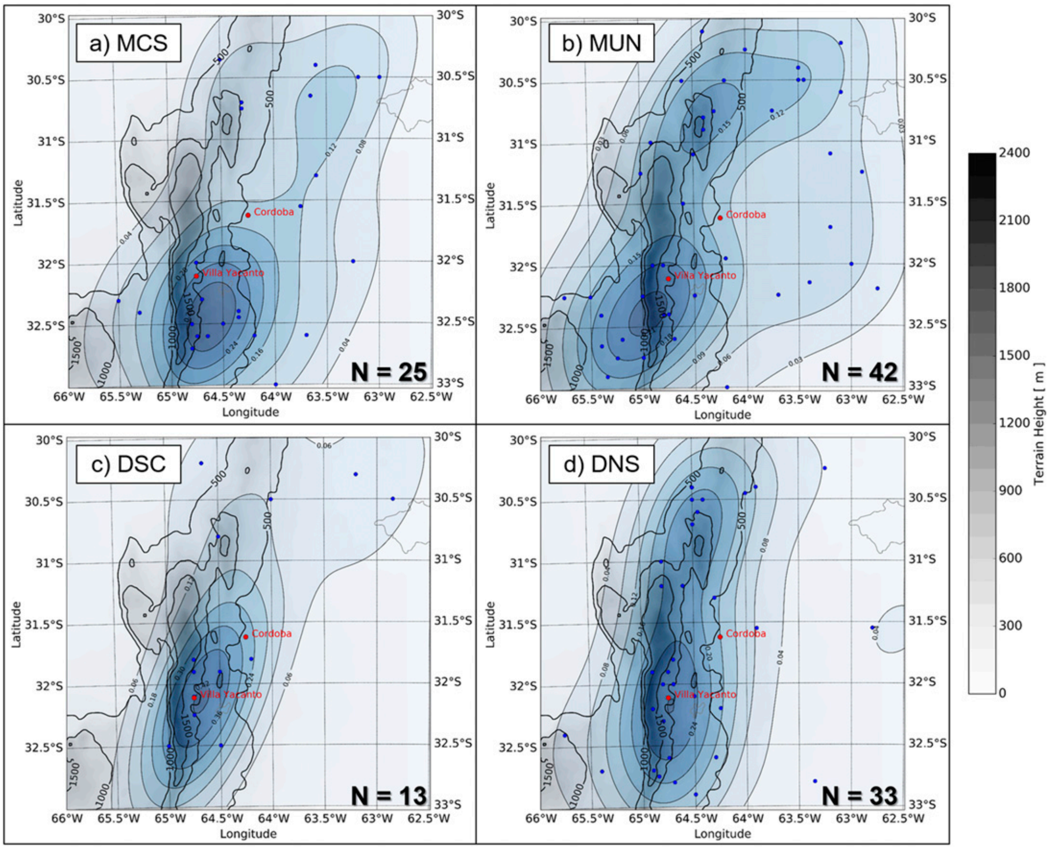

FIG. 6. As in Fig. 5, but by dominant convective mode: (a) MCS, (b) MUN, (c) DSC, and (d) DNS.

summer season (March/April; Fig. 9). This shift from discrete to multicellular convective modes agrees with the average positioning of the large-scale jet stream pattern, with a poleward shift in the jet stream observed during the transition from spring into summer (not shown) and resultant weaker vertical wind shear for more organized convective modes (e.g., supercells).

Of the 113 CI events, 31 (~27%) displayed distinctive upscale convective growth into an MCS. The three most prominent pathways for upscale convective growth were a transition from MUN to MCS (13 of the 31 events; ~42%), DNS to MCS (10 of the 31 events; ~32%), and DSC to MCS (eight of the 31 events; ~26%). This distribution in upscale convective growth by initial/dominant storm mode is similar to the study by Klimowski et al. (2004) in the United States (their Fig. 3). In contrast to the length of events (Fig. 10; left violin box plot), the distribution of time from CI to upscale convective growth was relatively short (~25% of total ''length of event'' distribution). This implies a rapid transition from CI to MCS over a fairly short duration of time (typically less than 3 h), which is important owing to the overlapping, and eventual transition in severe weather hazards between isolated and multicellular convective modes (e.g., Nielsen et al. 2015).

This implied rapid transition from CI to MCS is further supported by the spatial distribution of CI events and upscale convective growth locations depicted in Fig. 11. Upscale convective growth locations were defined as the centroid of the developing MCS when the system first met the aforementioned MCS criteria outlined in section 2. Upscale convective growth events were characterized by

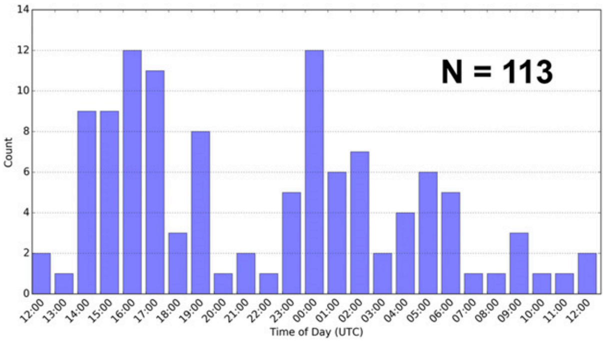

FIG. 7. Temporal distribution of CI times (UTC) for all convective modes.

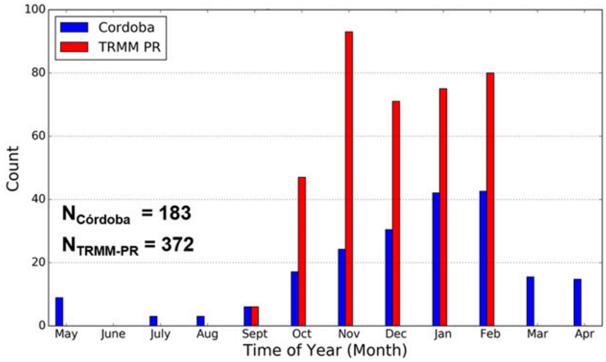

FIG. 8. Annual distribution of the number of events per month over the full 2-yr tracking period for Córdoba radar data, normalized by the number of days with available radar data per month (see text for details) and TRMM PR data.

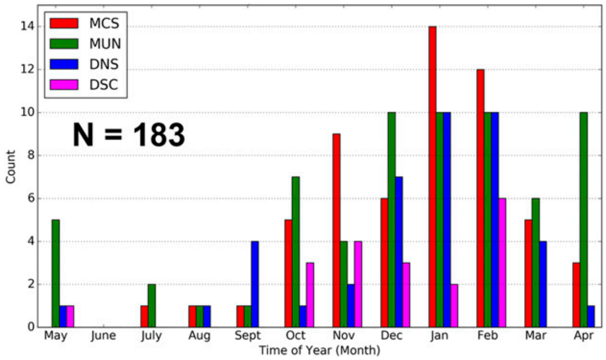

FIG. 9. As in Fig. 8, but by dominant convective mode: MCS, MUN, DNS, and DSC.

initial cell development across the SDC and then a rapid transition to MCS just downwind (east) of the terrain (near 32.25°S, 64.50°W). The distance between the approximate centroid of CI locations to upscale convective growth locations was ~25–50 km, which is much less than in the central United States (compared with Fig. 2 from Coniglio et al. 2010). One hypothesis is that as orogenic cells over the higher terrain move off to the east, they encounter an environment that is more supportive of rapid upscale convective growth. Another hypothesis is that deep convective storms continually develop over the SDC in association with prior cells that move east, off the terrain. This process of backbuilding convection has been highlighted before in this region via TRMM PR data (e.g., Rasmussen et al. 2014) and is noted in some of the upscale convective growth events identified using RMA1.

b. *Comparison with the TRMM PR*

To complement the RMA1 tracking results presented above, TRMM PR-observed convective systems were identified in the same radar tracking domain previously mentioned during the warm season (September–February) 1998–2014 time period. A total of 372 events were identified: 242 MCS (~65%), 76 discrete (~20%), and 54 MUN (~15%). These events were partitioned into DCCs (height of 40-dB*Z* echo >10 km) and WCCs (areal extent of 40-dB*Z* echo >1000 km^2) as well. These two categories were further separated between two time periods: SON (austral spring) and DJF (austral summer). A total of 145 (~39%) events were identified during the SON period, and 227 (~61%) events were identified during the DJF period (Table 3), which had a similar seasonal case partitioning, compared with the RMA1 results (Fig. 8; SON = ~29% and DJF = ~71%).

The distribution of discrete versus multicellular convective modes between RMA1 data and TRMM PR data are in good quantitative agreement. The results from RMA1 data depicted 60 discrete events (DSC and DNS combined; ~33%) and 123 multicell events (MCS and MUN combined; ~67%), whereas TRMM PR data depicted 76 discrete events (~20%) and 296 multicell events (MCS and MUN combined; ~80%). Owing to the relatively coarse horizontal resolution of the TRMM PR (~4–5 km), the discrete convective modes may be undersampled/spatially smoothed out, resulting in more multicell categorization in TRMM PR data than exists in reality (e.g., Heymsfield et al. 2000). Additionally, the TRMM PR tracking method removes the events that do not qualify as DCC or WCC, and thus, there are many more events that were not counted here that might explain this lower percentage of discrete storms. This discrepancy between RMA1 and TRMM PR data might also be true for the categorization between MUN and MCS events, with the MCS category dominating the TRMM PR statistics, whereas the MUN events are more prevalent in the RMA1 statistics. The TRMM PR algorithm for the WCC category requires that storms have a 40-dB*Z* echo >1000 km^2, potentially resulting in some missed MUN events. The length requirement for MCS events of the ≥30-dB*Z* echo (≥50 km) likely explains the higher counts of MCS events within the TRMM PR statistics, owing to the coarser horizontal resolution, compared with RMA1. Overall, DCCs tend to be associated more with discrete and MCS convective modes during the austral spring months (148 out of 169 total events; ~88%), with a transition to more MCS DCCs during the austral summer months. WCCs tend to almost exclusively be associated with multicellular convective modes (189 out of 203 total events; ~93%), which is not surprising, given the spatial requirements to be considered a WCC previously mentioned.

c. *Synoptic-scale composite analyses*

Storm environments supportive of the different ground-based, RMA1-identified convective modes were

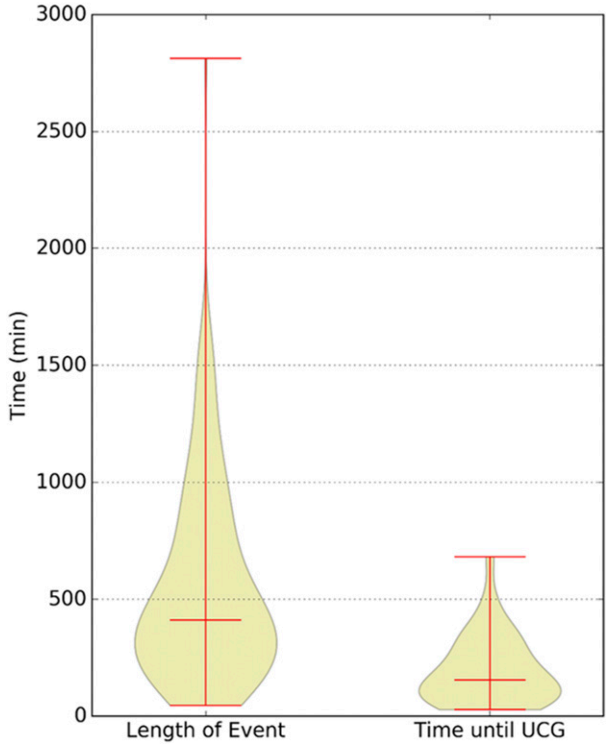

FIG. 10. Violin boxplots of length of event and time from CI until upscale convective growth (UCG; both in minutes).

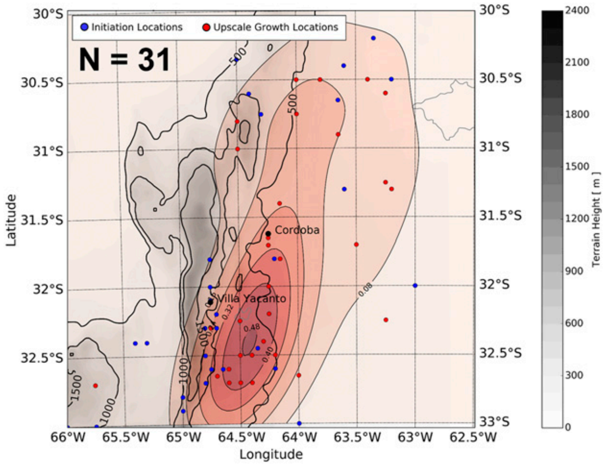

FIG. 11. Spatial distribution of all CI locations (blue dots) and UCG locations (red dots). A KDE (using Scott's rule; Scott 1992) of the upscale convective growth locations is denoted by red shades. The cities of Córdoba and Villa Yacanto are labeled in black. Terrain contours of 500, 1000, and 1500 m are outlined in thick black lines, and terrain height is shaded in gray (m).

constructed via 0.7° ERA-Interim data. Since ERA-Interim data are only available four times a day (0000, 0600, 1200, and 1800 UTC), the time closest (before or after) to CI was chosen to most accurately represent the near-storm environment. Only the 113 CI events, which include 42 MUN events, 33 DNS events, 25 MCS events, and 13 DSC events, were used to generate the following composites.

Both multicell categories (MCS and MUN) tend to be associated with strong flow aloft (>40 kt; 1 kt = 0.5144 m s^{-1}) with the core of the jet stream displaced to the southeast of the region for MCS events, potentially favoring synoptic-scale ascent (i.e., located within left entrance region of jet streak). MUN events are characterized by a northwesterly flow pattern aloft across the tracking domain (Fig. 12b), whereas MCS events display a more westerly component across the tracking domain (Fig. 12a). MUN events also tend to have a slightly more amplified upper-level trough off the west coast of South America, potentially resulting in greater quasigeostrophic (QG) forcing for synoptic-scale ascent or supporting frontal intrusions in some events, favoring more widespread CI. The largest differences in the upper-level patterns exist between DSC (Fig. 12c) and DNS (Fig. 12d) events. DSC events tend to be associated with strong flow aloft just upstream of the tracking domain (>50 kt) and a highly amplified upper-level trough to the southwest of central Chile. The core of the jet stream tends to be located just off the west coast of South America for DSC events, with the highest jet speeds impinging on the Andes Cordillera and the terminus of the jet streak over the SDC. This upper-level pattern favors lee troughing (e.g., Lichtenstein 1980; Seluchi et al. 2003; Saulo et al. 2004, 2007; Rasmussen and Houze 2016) and subsequent (possible) formation of a low-level jet owing to the indirect transverse ageostrophic secondary circulation at the terminus of the jet streak (e.g., Uccellini 1980). DNS events are characterized by the weakest flow aloft of all convective modes and subsequent weakest (implied) upper-level vertical wind shear.

All convective modes are associated with lee troughing and resultant northerly low-level flow, serving to transport moisture poleward from the Amazon rainforest region. The multicell categories tend to display a more pronounced LLJ signature that penetrates farther poleward than the discrete categories (cf. Figs. 13a,b

TABLE 3. Counts of TRMM PR-identified storms by convective mode, DCC vs WCC, and time of year (austral spring or summer).

Convective mode	DCC (spring)	WCC (spring)	DCC (summer)	WCC (summer)	Total
Discrete	29	6	33	8	76
MUN	13	14	8	19	54
MCS	29	54	57	102	242
Total	71	74	98	129	372

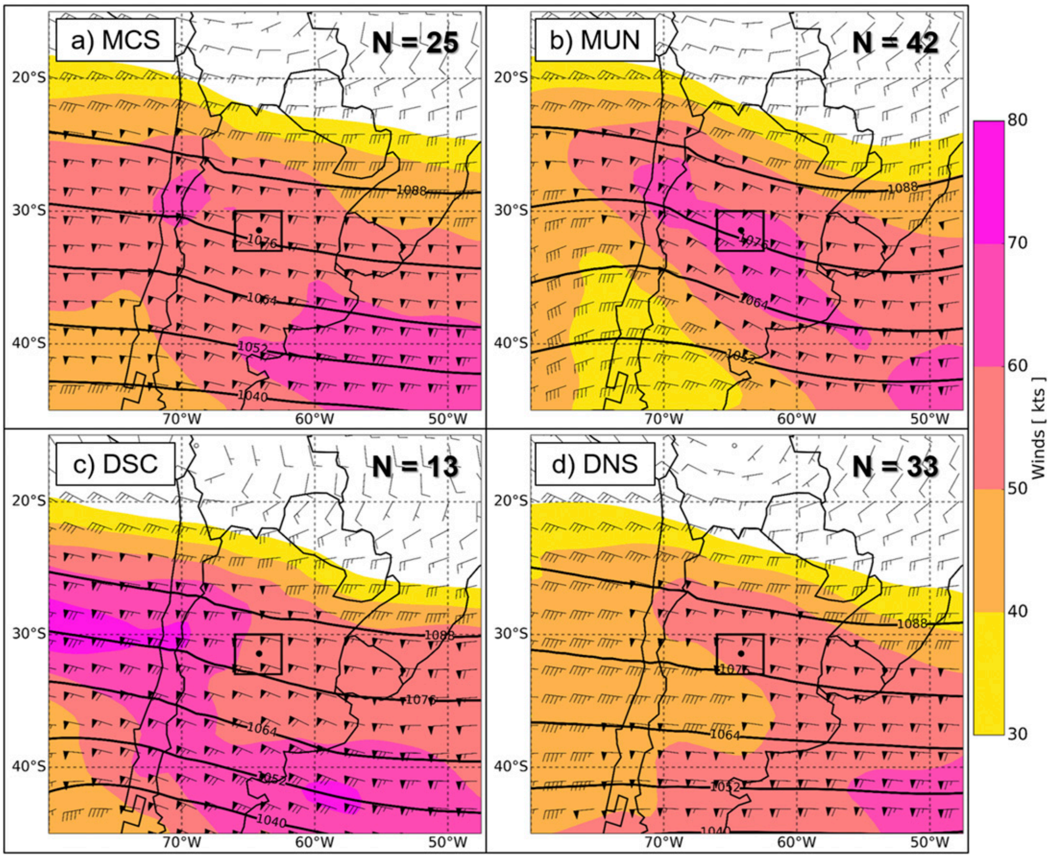

FIG. 12. ERA-Interim composite mean 250-hPa wind speed (shaded; kt), geopotential height (contoured in black every 12 dam), and wind barbs (half barb = 5 kt; full barb = 10 kt; pennant = 50 kt) for (a) MCS, (b) MUN, (c) DSC, and (d) DNS convective modes. The black square located in the center of each panel is the Córdoba radar tracking domain, and the black dot is the city of Córdoba.

with 13c,d). This results in more focused low-level moisture convergence near the SDC (not shown). The DSC events tend to have the greatest low-level moisture content near the Córdoba region, with mean 850-hPa specific humidity values of ~12–14 g kg^{-1}, and the strongest mean low-level wind speeds (>10 kt) within the tracking domain (Fig. 13c). The DNS events tend to have the weakest mean low-level flow and the lowest mean 850-hPa specific humidity values near the SDC (Fig. 13d). In comparison with the limited observations of the SALLJ, the ERA-Interim composites presented here generally depict a weaker low-level jet (Fig. 13; compared with results from Vera et al. 2006). Underestimation of the SALLJ may be due to the compositing procedure of a relatively large number of events per convective mode category.

d. *Environmental parameters*

Over the radar tracking domain, DSC events tend to have the greatest mean MLCAPE (~1000–2000 J kg^{-1}) and mean 0–6 km AGL vertical wind shear (~30–35 kt) of all the convective modes (Fig. 14c). This is consistent with Figs. 12c and 13c, which depict the strongest flow aloft and greatest low-level moisture content for DSC events. DSC events also display the greatest magnitudes of mean MLCAPE and mean vertical wind shear to the east of the SDC. The MUN events display the weakest mean MLCAPE, generally under ~750 J kg^{-1} (Fig. 14b). MCS events are similar to DSC events in their thermodynamic and kinematic environments, with average MLCAPE and shear magnitudes of ~1000–1500 J kg^{-1} and 30–35 kt, respectively (Fig. 14a). The local maximum in MLCAPE in the northwest corner of the 7° × 7° domain in both MCS and DSC composites likely owes to the greater low-level moisture evident in Figs. 13a and 13c. DNS events are characterized by MLCAPE magnitudes ~750–1250 J kg^{-1} and shear magnitudes ~25–30 kt, which is weaker than the other convective modes (Fig. 14d). All four convective modes display similar MLCIN magnitudes, with a local

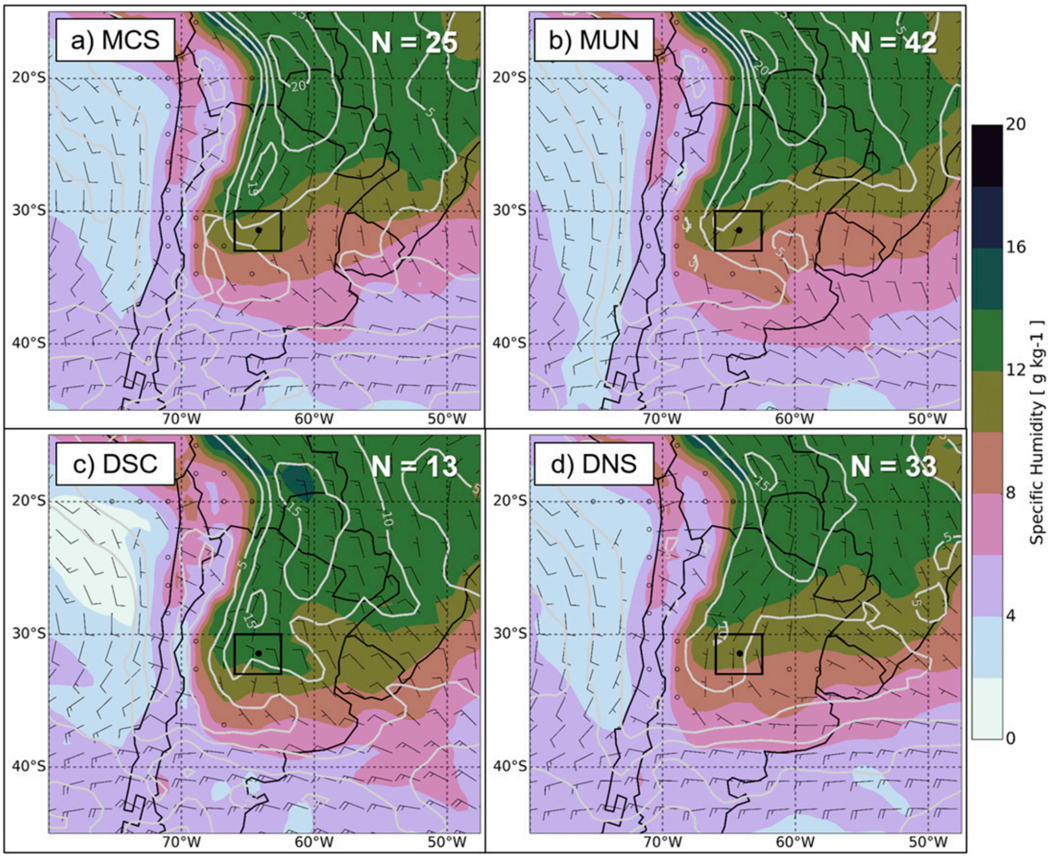

FIG. 13. As in Fig. 12, but for 850-hPa specific humidity (shaded; g kg^{-1}), isotachs (gray contours every 5 kt), and wind barbs (half barb = 5 kt; full barb = 10 kt; pennant = 50 kt).

minimum over the SDC, while MCS events (Fig. 14a) exhibit the strongest magnitudes of MLCIN to the north of the SDC.

Composite mean wind hodographs (constructed at a model grid point closest to Córdoba) for all convective modes are characterized by a veering of the vertical wind shear vector throughout the lower troposphere, indicative of low-level warm air/moisture advection (Fig. 15). These wind hodographs are similar to those constructed for the TRMM PR-identified storms presented in Rasmussen and Houze (2011) and in EML events identified by Ribeiro and Bosart (2018). DSC events display the greatest low-level hodograph curvature, whereas DNS events show the least amount; 0–3-km SRH magnitudes are greater for DSC events, as compared to DNS events as a result (~ −70 vs ~ −49 m^2 s^{-2}). MCS and MUN events display similar low-level hodographs; however, MUN events are characterized by a more northwest flow component aloft, in agreement with the upper-level pattern depicted in Fig. 12b. Similar west-northwest upper-level flow magnitudes (>40 kt) and subsequent deep-layer vertical wind shear magnitudes are apparent for each of the convective modes, with MCS environments characterized by the largest magnitudes of mean 0–6 km AGL vertical wind shear (~36 kt) and DNS environments the least (~30 kt).

ERA-Interim composite violin box plots were constructed by averaging quantities over a domain centered on the RMA1 site. MLCAPE magnitudes tend to be greatest for DSC events, with a median value ~1500 J kg^{-1} (Fig. 16a), similar to the results from Thompson et al. (2012) for supercell environments in the United States. Some DSC events, however, formed in environments with maximum MLCAPE magnitudes of >3500 J kg^{-1} (most unstable CAPE >6000 J kg^{-1}; not shown), likely supportive of the TRMM PR-identified DCCs (some 40-dB*Z* echo tops reaching >14 km AGL; not shown). MCS and DNS events have similar median MLCAPE magnitudes ~700 J kg^{-1}, whereas MUN events have the lowest MLCAPE magnitudes, with a median value ~300 J kg^{-1}. MLCIN magnitudes among the four convective modes tend to be similar across events, with an average median value ~−80 J kg^{-1}

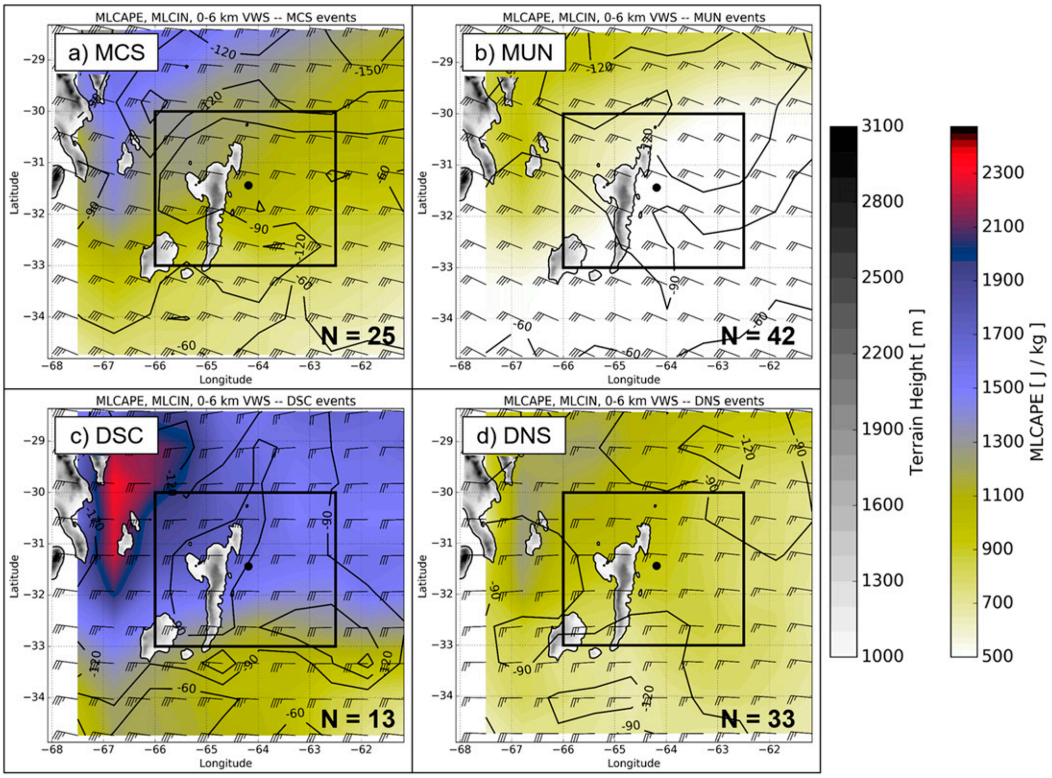

FIG. 14. ERA-Interim composite mean MLCAPE (shaded; J kg^{-1}), terrain height (shaded in gray; m), MLCIN (contoured in black every 30 J kg^{-1}), and 0–6-km AGL vertical wind shear (barbs; half barb = 5 kt; full barb = 10 kt; pennant = 50 kt) for (a) MCS, (b) MUN, (c) DSC, and (d) DNS convective modes. Elevation above 1000 m is shaded in gray, and the square black box located in the center of each panel is the Córdoba radar tracking domain.

(Fig. 16b). These magnitudes of MLCIN tend to be greater than their U.S. counterparts for supercell and MCS environments analyzed by Thompson et al. (2012; their Fig. 7) and fairly similar (within ~20 J kg^{-1}) to those associated with prominent EMLs across South America reported by Ribeiro and Bosart (2018; their Fig. 15b).

Mixed-layer lifting condensation-level (MLLCL; averaged over the lowest 100 hPa) heights for the four convective modes are depicted in Fig. 16c. MUN events tend to have the lowest MLLCL heights, with a median value ~1000 m. MCS, DSC, and DNS events have similar median values of MLLCL heights, with an average ~1300 m. The DSC events have similar MLLCL heights as the U.S. analyzed supercell storms; however, MCS events display slightly higher MLLCL heights in the South American–analyzed storms [compared with Fig. 6 from Thompson et al. (2012)]. The higher average MLLCL heights in these MCS environments may be supportive of more subcloud evaporation, potentially fostering more rapid upscale convective growth via cold pool amalgamation.

Deep-layer vertical wind shear (0–6 km AGL) magnitudes among the four convective modes are similar, with median values ranging from ~30 to 40 kt (Fig. 16d). These median values of vertical wind shear tend to be weaker than in U.S. storm environments, specifically for MCS and DSC events (e.g., Thompson et al. 2012). The 0–3-km SRH magnitudes among the four convective modes are fairly similar, with a median value of ~−65 m^2 s^{-2} (Fig. 16e). MCS and MUN environments tend to have the largest 0–3-km SRH magnitudes (~−300 to −250 m^2 s^{-2}), likely owing to the stronger SALLJ in these events (e.g., Fig. 13a). DSC events have maximum SRH magnitudes of ~ −150 m^2 s^{-2}. DNS and MUN events display large spread of SRH, with values ranging from ~−300 to 30 m^2 s^{-2}. The magnitudes of 0–1-km SRH (specifically for MCS and DSC events) tend to be much lower than their U.S. counterparts (Fig. 16f; e.g., Thompson et al. 2012), which might assist in the explanation of the observed rapid upscale convective growth of orogenic convection into MCSs for some events. Incipient convective outflows may be unable to stay restricted to their parent storm in these

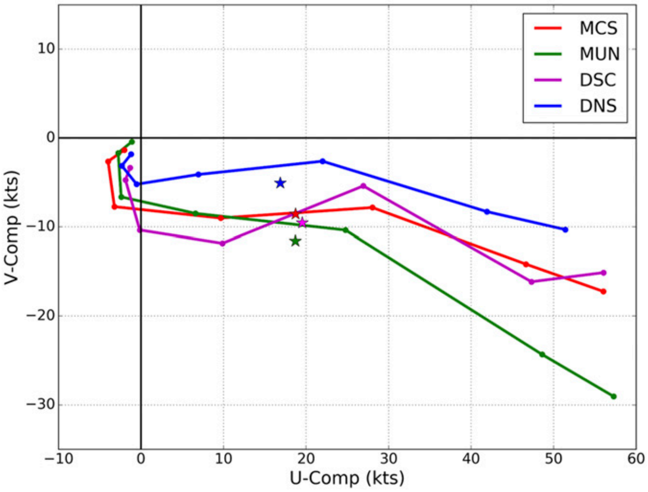

Mean 0–6 km AGL vertical wind shear:
MCS = 36 kts
MUN = 34 kts
DSC = 32 kts
DNS = 30 kts

Mean 0–3 km AGL storm-relative helicity:
MCS = -96 $m^2 s^{-2}$
MUN = -89 $m^2 s^{-2}$
DSC = -70 $m^2 s^{-2}$
DNS = -49 $m^2 s^{-2}$

Mean 0–1 km AGL storm-relative helicity:
MCS = -27 $m^2 s^{-2}$
MUN = -32 $m^2 s^{-2}$
DSC = -19 $m^2 s^{-2}$
DNS = -10 $m^2 s^{-2}$

FIG. 15. ERA-Interim composite mean wind hodographs for MCS, MUN, DSC, and DNS convective modes. The x axis is the u component of the wind (kt), and the y axis is the v component of the wind (kt). Dots represent the following pressure levels: 1000, 925, 850, 700, 500, 300, and 250 hPa. Average storm motions, calculated using the mean wind between 1000 and 250 hPa, are labeled with stars. (top) The 0–6-km AGL mean vertical wind shear (kt), (middle) 0–3-km AGL SRH ($m^2 s^{-2}$), and (bottom) 0–1-km AGL SRH ($m^2 s^{-2}$) magnitudes for the four different dominant convective modes.

weaker low-level flow/shear environments, fostering more rapid upscale convective growth than the U.S. observed storms (see Figs. 10, 11).

4. Summary and conclusions

Satellite observations have revealed that some of the world's most intense convective storms on Earth occur in northern and central Argentina, South America, typically displaying deep and wide convective cores, and are associated with the full range of severe weather hazards. Past studies have characterized the frequency and three-dimensional characteristics of these convective storms using TRMM PR data; however, these data were unable to discern the temporal evolution of convection and distinguish supercell from nonsupercell storms. A newly installed C-band, dual-polarization Doppler weather radar located in the city of Córdoba has allowed for characterization of common convective modes across a region surrounding the northern SDC.

A total of 183 events were identified between May 2015 and May 2017, with nearly two-thirds of these events characterized as multicell convective storms. Most convection initiates preferentially in two parts of the SDC (on the high central terrain and the northern tip) and subsequently tracks eastward. There are two distinct peaks of CI time, with one in the late morning/early afternoon hours (1100–1600 LST) and another around sunset (2000–0300 LST). The annual cycle reveals that the most active months for deep convective storms near the SDC are between November and February or during the transition from austral spring into summer. Discrete convective modes tend to be favored earlier in the austral spring season, whereas multicellular convective modes are skewed toward later in the spring season and into the summer season.

The overall characterization of convection into multicellular (MCS and MUN combined) versus discrete (DSC and DNS combined) convective modes between RMA1 data and TRMM PR data are fairly consistent (within 10%–15% occurrence fraction of each other). Both radars reveal that most events are binned into the multicell categories (≥67%), whereas a smaller fraction of events are binned into the discrete category (≤33%). Both RMA1 data and TRMM PR data reveal that most events occur between December and February (≥69%; austral summer) with fewer between September and November (≤31%; austral spring).

Of the 113 events that had CI within the domain and had radar data available at the time of CI, 31 (~27%) displayed distinctive upscale convective growth into an MCS. Upscale convective growth tends to occur relatively fast, compared with the central United States, usually within the first 3 h following CI, and occurs relatively close and to the east of the steepest gradient in terrain in the central SDC. Ongoing work utilizing high-resolution

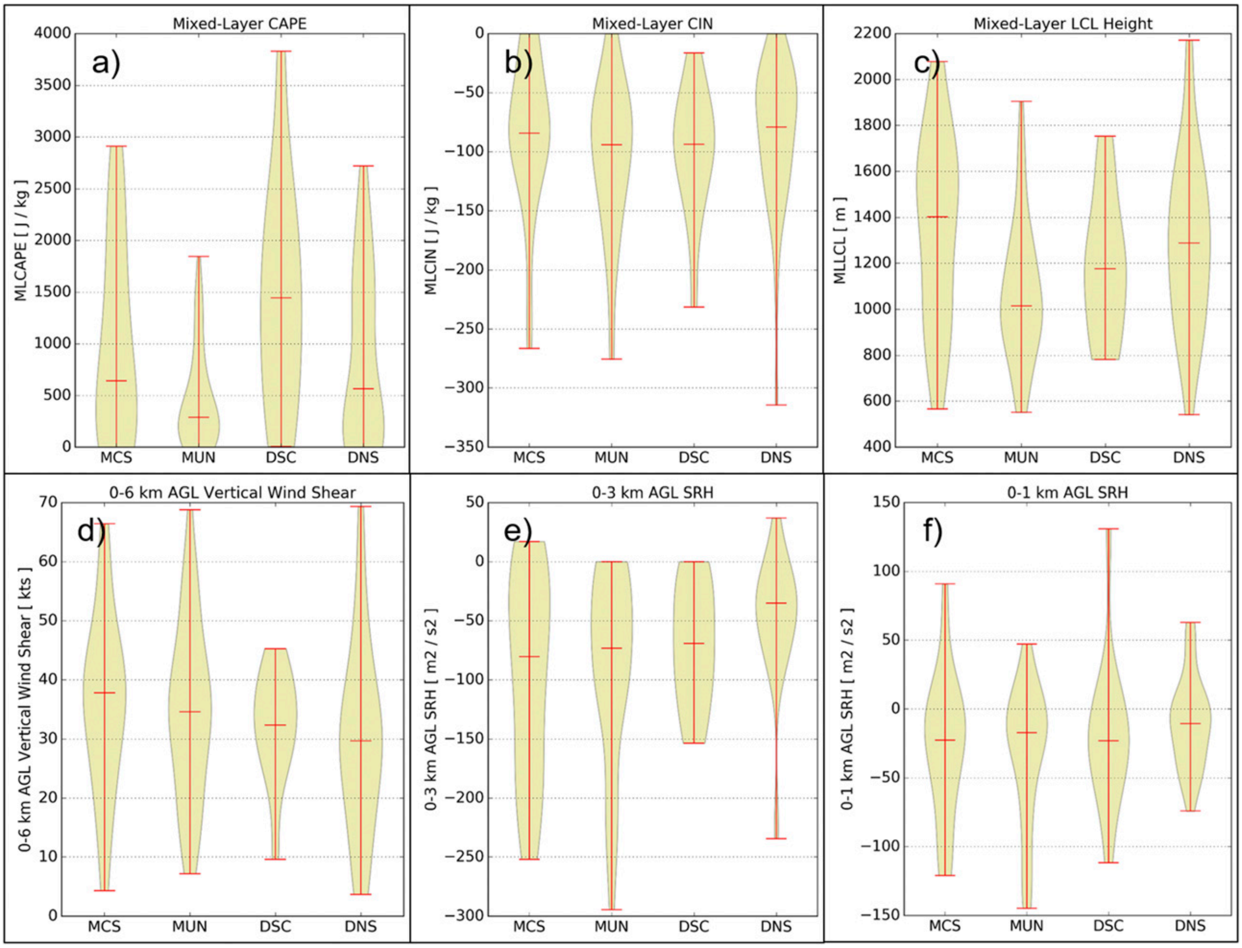

FIG. 16. ERA-Interim composite mean violin boxplots averaged over a 3° × 3.5° (30°–33°S, 62.5°–66°W) domain for (a) MLCAPE ($\mathrm{J\,kg^{-1}}$), (b) MLCIN ($\mathrm{J\,kg^{-1}}$), (c) MLLCL height (m), (d) 0–6-km AGL vertical wind shear (kt), (e) 0–3-km AGL SRH ($\mathrm{m^2\,s^{-2}}$), and (f) 0–1-km AGL SRH ($\mathrm{m^2\,s^{-2}}$).

numerical modeling is underway to investigate the mechanisms for this relatively fast transition from first storms to MCSs, as this process has sensible weather impacts, such as severe weather hazard type.

ERA-Interim composites were constructed for the different convective modes identified by the Córdoba radar. All convective modes are typically associated with strong upper-level westerly flow, with DSC events exhibiting the strongest upstream flow fields. The largest-amplitude (upstream) upper-level trough tends to occur during MUN events, where removal of any capping inversion is hypothesized to lead to widespread CI. The low-level environments among the four different modes are generally similar, despite DSC events displaying more moisture than the other convective modes, and are characterized by lee-side troughing, owing to the westerly flow aloft over the Andes Cordillera, and subsequent poleward intrusions of warm/moist air from the Amazon rainforest region. Low-level winds and moisture content tend to be greatest in DSC environments, whereas the strongest (upstream) low-level jet feature is associated with MCS and MUN environments.

Composites of MLCAPE and deep-layer vertical wind shear reveal that DSC events comprise large magnitudes of both severe weather parameters, over a widespread west-to-east region near the SDC. Compared with U.S. environments supportive of MCSs and DSCs, Argentina storm environments generally display larger magnitudes of MLCAPE and MLCIN, weaker low-level shear/SRH, and higher MLLCL heights. The generally weaker low-level shear and higher MLLCL heights constituting these environments may be possible factors in the observed fast transition from first storms to MCSs previously described. One caveat of this analysis, beyond inherent resolution issues and biases in any reanalysis product, is the ability of ERA-Interim to resolve the impacts of complex terrain near the SDC on flow and thermodynamic fields related to deep convective life cycle, which can only be ameliorated by additional observations.

Data from the Remote Sensing of Electrification, Lightning, and Mesoscale/Microscale Processes with Adaptive Ground Observations (RELAMPAGO) field campaign, to be conducted between 1 November and 15 December 2018 (https://publish.illinois.edu/relampago/), will be used to address hypotheses posed herein. This field campaign will document the intense convective storms via a multitude of observing platforms, including, but not limited to three mobile Doppler-on-Wheels radars (Wurman et al. 1997), fixed radar sites, the Department of Energy Atmospheric Radiation Measurement Climate Research Facility Gulfstream-I aircraft (Schmid et al. 2014), mobile and fixed rawinsondes, and mobile mesonets and pods, among others. These data will enhance our understanding of the processes regulating some of the world's most intense deep convective storms near the unique terrain of the SDC.

Acknowledgments. The authors thank Jim Wilson and Rita Roberts (National Center for Atmospheric Research) and Robert Rauber and Deanna Hence (University of Illinois at Urbana–Champaign; UIUC) for fruitful discussion and Benjamin Vega-Westhoff, Chuan-Chieh Chang, and Tzu-shun Lin (UIUC) for computing assistance. The authors would also like to thank editor Dr. Pam Heinselman and two reviewers for improving this manuscript. Many thanks go to Janice Mulholland for her useful comments improving this manuscript. Support for this work was made possible by National Science Foundation Grants AGS-1661799 for the first and second authors, AGS-1661800 for the third author, and AGS-1661657 for the fourth author.

REFERENCES

Bluestein, H. B., and M. H. Jain, 1985: Formation of mesoscale lines of precipitation: Severe squall lines in Oklahoma during the spring. *J. Atmos. Sci.*, **42**, 1711–1732, https://doi.org/10.1175/1520-0469(1985)042<1711:FOMLOP>2.0.CO;2.

Blumberg, W. G., K. T. Halbert, T. A. Supinie, P. T. Marsh, R. L. Thompson, and J. A. Hart, 2017: SHARPpy: An open-source sounding analysis toolkit for the atmospheric sciences. *Bull. Amer. Meteor. Soc.*, **98**, 1625–1636, https://doi.org/10.1175/BAMS-D-15-00309.1.

Bonner, W. D., 1968: Climatology of the low level jet. *Mon. Wea. Rev.*, **96**, 833–850, https://doi.org/10.1175/1520-0493(1968)096<0833:COTLLJ>2.0.CO;2.

Brooks, H., C. A. Doswell III, and M. P. Kay, 2003: Climatological estimates of local daily tornado probability for the United States. *Wea. Forecasting*, **18**, 626–640, https://doi.org/10.1175/1520-0434(2003)018<0626:CEOLDT>2.0.CO;2.

Cecil, D. J., and C. B. Blankenship, 2012: Toward a global climatology of severe hailstorms as estimated by satellite passive microwave imagers. *J. Climate*, **25**, 687–703, https://doi.org/10.1175/JCLI-D-11-00130.1.

Coniglio, M. C., J. Y. Hwang, and D. J. Stensrud, 2010: Environmental factors in the upscale growth and longevity of MCSs derived from Rapid Update Cycle analyses. *Mon. Wea. Rev.*, **138**, 3514–3539, https://doi.org/10.1175/2010MWR3233.1.

Davies-Jones, R., 1984: Streamwise vorticity: The origin of updraft rotation in supercell storms. *J. Atmos. Sci.*, **41**, 2991–3006, https://doi.org/10.1175/1520-0469(1984)041<2991:SVTOOU>2.0.CO;2.

Dee, D. P., and Coauthors, 2011: The ERA-Interim reanalysis: Configuration and performance of the data assimilation system. *Quart. J. Roy. Meteor. Soc.*, **137**, 553–597, https://doi.org/10.1002/qj.828.

Dial, G. L., J. P. Racy, and R. L. Thompson, 2010: Short-term convective mode evolution along synoptic boundaries. *Wea. Forecasting*, **25**, 1430–1446, https://doi.org/10.1175/2010WAF2222315.1.

Doswell, C. A., III, H. E. Brooks, and R. A. Maddox, 1996: Flash flood forecasting: An ingredients-based methodology. *Wea. Forecasting*, **11**, 560–581, https://doi.org/10.1175/1520-0434(1996)011<0560:FFFAIB>2.0.CO;2.

Fabry, F., 2015: *Radar Meteorology: Principles and Practice.* Cambridge University Press, 256 pp.

Gallus, W. A., N. A. Snook, and E. V. Johnson, 2008: Spring and summer severe weather reports over the Midwest as a function of convective mode: A preliminary study. *Wea. Forecasting*, **23**, 101–113, https://doi.org/10.1175/2007WAF2006120.1.

Helmus, J. J., and S. M. Collis, 2016: The Python ARM Radar Toolkit (Py-ART), a library for working with weather radar data in the Python programming language. *J. Open Res. Software*, **4**, e25, https://doi.org/10.5334/jors.119.

Heymsfield, G. M., B. Geerts, and L. Tian, 2000: TRMM precipitation radar reflectivity profiles as compared with high-resolution airborne and ground-based radar measurements. *J. Appl. Meteor.*, **39**, 2080–2102, https://doi.org/10.1175/1520-0450(2001)040<2080:TPRRPA>2.0.CO;2.

Houze, R. A., Jr., B. F. Smull, and P. Dodge, 1990: Mesoscale organization of springtime rainstorms in Oklahoma. *Mon. Wea. Rev.*, **118**, 613–654, https://doi.org/10.1175/1520-0493(1990)118<0613:MOOSRI>2.0.CO;2.

——, D. C. Wilton, and B. F. Smull, 2007: Monsoon convection in the Himalayan region as seen by the TRMM precipitation radar. *Quart. J. Roy. Meteor. Soc.*, **133**, 1389–1411, https://doi.org/10.1002/qj.106.

——, K. L. Rasmussen, M. D. Zuluaga, and S. R. Brodzik, 2015: The variable nature of convection in the tropics and subtropics: A legacy of 16 years of the Tropical Rainfall Measuring Mission satellite. *Rev. Geophys.*, **53**, 994–1021, https://doi.org/10.1002/2015RG000488.

Johns, R. H., and C. A. Doswell, 1992: Severe local storms forecasting. *Wea. Forecasting*, **7**, 588–612, https://doi.org/10.1175/1520-0434(1992)007<0588:SLSF>2.0.CO;2.

Johnson, R. H., and B. E. Mapes, 2001: Mesoscale processes and severe convective weather. *Severe Convective Storms*, *Meteor. Monogr.*, No. 50, Amer. Meteor. Soc., 71–122, https://doi.org/10.1175/0065-9401-28.50.71.

Klimowski, B. A., M. R. Hjelmfelt, and M. J. Bunkers, 2004: Radar observations of the early evolution of bow echoes. *Wea. Forecasting*, **19**, 727–734, https://doi.org/10.1175/1520-0434(2004)019<0727:ROOTEE>2.0.CO;2.

Kummerow, C., W. Barnes, T. Kozu, J. Shiue, and J. Simpson, 1998: The Tropical Rainfall Measuring Mission (TRMM) sensor package. *J. Atmos. Oceanic Technol.*, **15**, 809–817, https://doi.org/10.1175/1520-0426(1998)015<0809:TTRMMT>2.0.CO;2.

Lichtenstein, E. R., 1980: La depresion del Noroeste Argentino (The northwestern Argentina low). Ph.D. dissertation, Ciudad Universitaria, 223 pp.

Markowski, P. M., and Y. P. Richardson, 2014: The influence of environmental low-level shear and cold pools on tornadogenesis: Insights from idealized simulations. *J. Atmos. Sci.*, **71**, 243–275, https://doi.org/10.1175/JAS-D-13-0159.1.

——, J. M. Straka, and E. N. Rasmussen, 2002: Direct surface thermodynamic observations within the rear-flank downdrafts of nontornadic and tornadic supercells. *Mon. Wea. Rev.*, **130**, 1692–1721, https://doi.org/10.1175/1520-0493(2002)130<1692:DSTOWT>2.0.CO;2.

Nesbitt, S. W., R. Cifelli, and S. A. Rutledge, 2006: Storm morphology and rainfall characteristics of TRMM precipitation features. *Mon. Wea. Rev.*, **134**, 2702–2721, https://doi.org/10.1175/MWR3200.1.

Nielsen, E. R., G. R. Herman, R. C. Tournay, J. M. Peters, and R. S. Schumacher, 2015: Double impact: When both tornadoes and flash floods threaten the same place at the same time. *Wea. Forecasting*, **30**, 1673–1693, https://doi.org/10.1175/WAF-D-15-0084.1.

Rasmussen, K. L., and R. A. Houze Jr., 2011: Orogenic convection in subtropical South America as seen by the TRMM satellite. *Mon. Wea. Rev.*, **139**, 2399–2420, https://doi.org/10.1175/MWR-D-10-05006.1.

——, and ——, 2016: Convective initiation near the Andes in subtropical South America. *Mon. Wea. Rev.*, **144**, 2351–2374, https://doi.org/10.1175/MWR-D-15-0058.1.

——, M. D. Zuluaga, and R. A. Houze, 2014: Severe convection and lighting in subtropical South America. *Geophys. Res. Lett.*, **41**, 7359–7366, https://doi.org/10.1002/2014GL061767.

Rauber, R. M., and S. W. Nesbitt, 2018: *Radar Meteorology, an Introduction*. Wiley Blackwell, 461 pp.

Repinaldo, H. F. B., M. Nicolini, and Y. G. Skabar, 2015: Characterizing the diurnal cycle of low-level circulation and convergence using CFSR data in southeastern South America. *J. Appl. Meteor. Climatol.*, **54**, 671–690, https://doi.org/10.1175/JAMC-D-14-0114.1.

Ribeiro, B. Z., and L. F. Bosart, 2018: Elevated mixed layers and associated severe thunderstorm environments in South and North America. *Mon. Wea. Rev.*, **146**, 3–28, https://doi.org/10.1175/MWR-D-17-0121.1.

Romatschke, U., and R. A. Houze Jr., 2010: Extreme summer convection in South America. *J. Climate*, **23**, 3761–3791, https://doi.org/10.1175/2010JCLI3465.1.

Salio, P., M. Nicolini, and E. J. Zipser, 2007: Mesoscale convective systems over southeastern South America and their relationship with the South American low-level jet. *Mon. Wea. Rev.*, **135**, 1290–1309, https://doi.org/10.1175/MWR3305.1.

Saulo, A. C., M. E. Seluchi, and M. Nicolini, 2004: A case study of a Chaco low-level jet event. *Mon. Wea. Rev.*, **132**, 2669–2683, https://doi.org/10.1175/MWR2815.1.

——, J. Ruiz, and Y. G. Skabar, 2007: Synergism between the low-level jet and organized convection at its exit region. *Mon. Wea. Rev.*, **135**, 1310–1326, https://doi.org/10.1175/MWR3317.1.

Schmid, B., and Coauthors, 2014: The DOE ARM Aerial Facility. *Bull. Amer. Meteor. Soc.*, **95**, 723–742, https://doi.org/10.1175/BAMS-D-13-00040.1.

Schumann, M. R., and P. J. Roebber, 2010: The influence of upper-tropospheric potential vorticity on convective morphology. *Mon. Wea. Rev.*, **138**, 463–474, https://doi.org/10.1175/2009MWR3091.1.

Scott, D. W., 1992: *Multivariate Density Estimation: Theory, Practice, and Visualization*. John Wiley & Sons, 336 pp.

Seluchi, M. E., A. C. Saulo, M. Nicolini, and P. Satyamurty, 2003: The northwestern Argentinean low: A study of two typical events. *Mon. Wea. Rev.*, **131**, 2361–2378, https://doi.org/10.1175/1520-0493(2003)131<2361:TNALAS>2.0.CO;2.

Smith, B. T., R. L. Thompson, J. S. Grams, C. Broyles, and H. E. Brooks, 2012: Convective modes for significant severe thunderstorms in the contiguous United States. Part I: Storm classification and climatology. *Wea. Forecasting*, **27**, 1114–1135, https://doi.org/10.1175/WAF-D-11-00115.1.

Thompson, R. L., R. Edwards, J. A. Hart, K. L. Elmore, and P. Markowski, 2003: Close proximity soundings within supercell environments obtained from the Rapid Update Cycle. *Wea. Forecasting*, **18**, 1243–1261, https://doi.org/10.1175/1520-0434(2003)018<1243:CPSWSE>2.0.CO;2.

——, B. T. Smith, J. S. Grams, A. R. Dean, and C. Broyles, 2012: Convective modes for significant severe thunderstorms in the contiguous United States. Part II: Supercell and QLCS tornado environments. *Wea. Forecasting*, **27**, 1136–1154, https://doi.org/10.1175/WAF-D-11-00116.1.

Trapp, R. J., 2013: *Mesoscale-Convective Processes in the Atmosphere.* Cambridge University Press, 346 pp.

——, S. A. Tessendorf, E. S. Godfrey, and H. E. Brooks, 2005: Tornadoes from squall lines and bow echoes. Part I: Climatological distribution. *Wea. Forecasting*, **20**, 23–34, https://doi.org/10.1175/WAF-835.1.

Uccellini, L. W., 1980: On the role of upper tropospheric jet streaks and leeside cyclogenesis in the development of low-level jets in the Great Plains. *Mon. Wea. Rev.*, **108**, 1689–1696, https://doi.org/10.1175/1520-0493(1980)108<1689:OTROUT>2.0.CO;2.

Vera, C., and Coauthors, 2006: The South American low-level jet experiment. *Bull. Amer. Meteor. Soc.*, **87**, 63–78, https://doi.org/10.1175/BAMS-87-1-63.

Wurman, J., J. Straka, E. Rasmussen, M. Randall, and A. Zahrai, 1997: Design and deployment of a portable, pencil-beam, pulsed, 3-cm Doppler radar. *J. Atmos. Oceanic Technol.*, **14**, 1502–1512, https://doi.org/10.1175/1520-0426(1997)014<1502:DADOAP>2.0.CO;2.

Zipser, E. J., D. J. Cecil, C. Liu, S. W. Nesbitt, and D. P. Yorty, 2006: Where are the most intense thunderstorms on Earth? *Bull. Amer. Meteor. Soc.*, **87**, 1057–1072, https://doi.org/10.1175/BAMS-87-8-1057.